Defocus leakage radiation microscopy for single shot surface plasmon measurement

OPEN ACCESS
IOP Publishing
Measurement Science and Technology
Meas. Sci. Technol. **31** (2020) 075401 (8pp)
https://doi.org/10.1088/1361-6501/ab7def

Defocus leakage radiation microscopy for single shot surface plasmon measurement

Terry W K Chow[1], Daniel P K Lun[1], Suejit Pechprasarn[2,3] and Michael G. Somekh[2,4]

[1] Department of Electronics and Information Engineering, The Hong Kong Polytechnic University, Hung Hom, Hong Kong
[2] Center for Nanophotonics, Shenzhen University, Shenzhen PRC 518060, People's Republic of China
[3] College of Biomedical Engineering, Rangsit University, Pathum Thani 12000, Thailand
[4] Faculty of Engineering, University of Nottingham, Nottingham NG7 2RD, United Kingdom

E-mail: mike.somekh@szu.edu.cn

Received 6 July 2019, revised 25 February 2020
Accepted for publication 9 March 2020
Published 24 April 2020

Abstract

Measurement of surface plasmon and surface wave propagation is important for the operation and characterization of sensors and microscope systems. One challenge is to perform these measurements both quickly and with good spatial resolution without any modification to the sample surface. This paper addresses these issues by projecting an image of the field excited from a defocused sample to a magnified image plane. By carefully analysing the intensity distribution in this plane the properties of the surface waves generated on the sample surface can be determined. This has the advantage over previous techniques that the data can be obtained in a single shot without any changes to the focal position of the sample. Equally importantly, we show the method measures the local properties of the sample at well-defined positions, whereas other methods such as direct observation of the back focal plane average the properties over the propagation length of the surface waves.

Keywords: surface plasmon, single shot, image plane

(Some figures may appear in colour only in the online journal)

1. Introduction

Visualization and measurement of surface wave and surface plasmon (SP) propagation on a local scale with a microscope objective [1] can provide insight into the properties of SPs and become the basis for novel sensing and microscopy techniques [2, 3]. In the present paper we present a method that can measure SP properties, such as wavelength and attenuation, on a local scale, which, compared to previous approaches is very rapid performing the measurement in a single shot, which is important when trying to assess samples whose properties change in time such as biomolecules.

It is important to clarify what we mean by localized measurements. Traditional prism based SP methods, using the Kretschmann configuration [4], have lateral resolution limited to a few times the propagation length of the SPs. Typically, in the visible region the decay length of the field is several microns on gold, depending on the wavelength [5]. We wish to obtain resolution an order of magnitude better than this in order to probe the sample properties much more finely. Near field probe measurements have excellent resolution and have been around for a long time [6] but these are slow and require access to the sample surface. In order to make a quantitative tool applicable for routine measurement there is considerable advantage in using a system employing only far field optics without modification to the sample.

One approach to obtain localized measurements is to utilize the so-called $V(z)$ effect where the output of a heterodyne interferometer is recorded as the defocus of the sample, z, is

changed [2, 3]. In these systems a high numerical aperture oil immersion lens is used to excite the SPs, and detect the light reradiated back as the SPs are converted to propagating light in the coupling fluid. At negative defocus (corresponding the sample moved closer to the microscope objective) there is an interference signal between a reference beam incident close to the normal and the part of the field incident around the angle for excitation of surface waves. The defocus, z, is then changed so that an interference signal between the light reflected at normal incidence and light involving excitation and reradiation of surface waves occurs. The period of the interference signal measured of over a range of negative defocus values gives a measure of the wave vector and the attenuation of the SPs. In later work the heterodyne interferometer was replaced by a confocal microscope [7], which has a similar response but is simpler to implement experimentally. The reason for the localization of the signal in the confocal (and heterodyne interferometer) is that although the light converted to SPs reradiates continuously, the confocal arrangement ensures that only the light that appears to come from the focus of the microscope is detected [8]. In effect, light reradiated from other positions misses the confocal pinhole. The most effective way to recover the surface wave k-vector is to determine the phase of the interference signal as a function of defocus. The gradient of this phase change can be readily used to determine the desired surface wave properties [8]. In [8] and subsequent papers a spatial light modulator (SLM) was used to perform phase stepping between the two wave contributions, which allowed the variation of phase with defocus to be determined. Although this method was very effective it required the use of an expensive SLM to impose the phase stepping. Moreover, the switching speed of the SLM imposed a limitation on the data acquisition speed. There is therefore great merit if the phase can be reconstructed with a smaller number of measurements. One method to do this is to apply a Hilbert transform to the windowed $V(z)$ curve [9]. This means that the k-vector of the surface wave can be recovered without phase stepping although variation of the defocus is still necessary. This defocus variation can be achieved with physical defocus or by using the SLM to impose the appropriate phase profile. Single shot measurements of the SP propagation at a single focal position can be obtained with a different approach namely measurement of the reflection on the BFP [10], however, towards the end of the paper we analyze and discuss the limitations of this method compared to the image plane analysis we describe here and show that considerably better localization of the measurement may be achieved with image plane analysis.

The present paper takes a different approach to previous work by operating at a single defocus position, thus removing the need to perform measurements at different defocuses. Moreover, the method we present does not require phase stepping. The key idea in the present paper is to examine the intensity distribution in the image plane. Previously, we used multiple defocus positions and point detection in the image plane, here we reverse the situation examining the imaging field with array detection at a single defocus.

In order to better understand the process, we will be specific and consider a simplified schematic diagram (omitting the illumination path) of the system used in this study (see figure 1(a)). It should be noted that both excitation and detection occur below the sample, so there is no optics above the sample allowing complete separation between the sensing region and the sensor as shown in figure 1(d). This is very important in sensing applications as there is no optics to disturb the measurement process.

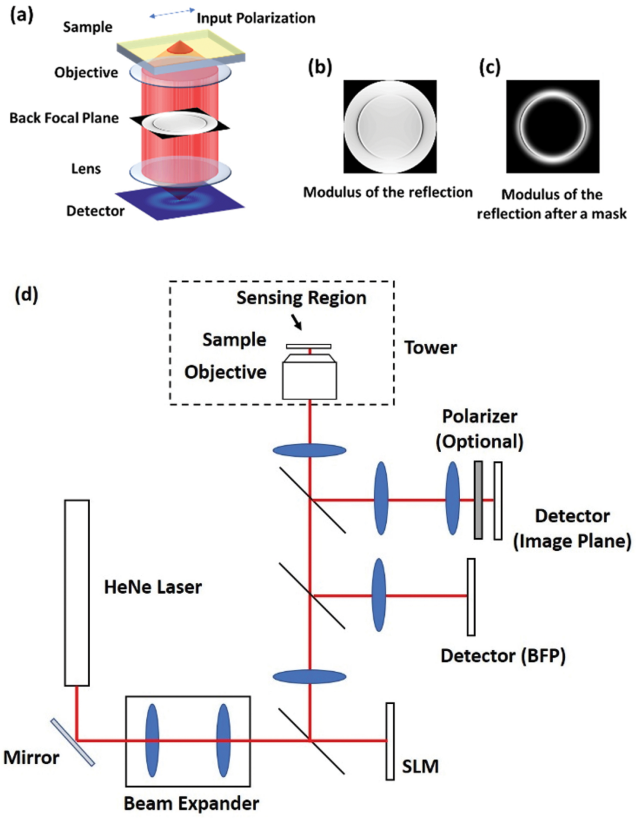

Figure 1. (a) Simplified schematic of the image plane visualization system. (b) Typical back focal plane distribution. (c) Masked region around region of SP excitation projected to the image plane. (d) Full schematic of the measurement system. The tower represents vertically aligned components to allow fluid to be placed in the sensing region.

Other publications have reported the use of the image plane to examine the emission of SPs, however, these works generally used fluorescence from point emitters [11] or scattering from point objects [1, 12]. In these cases excitation of SPs occurs above the sample with a separate optical system above the gold sample which as mentioned in the previous paragraph is much less convenient for construction of a sensor since it obstructs the sensing region. Zhang *et al* [13] excited the SPs using an objective with no additional scatterers, however, they did not defocus the excitation beam which meant their source was more point-like, whereas the one we used in the present paper is essentially a ring on account of the sample defocus as discussed later. This makes a crucial change to the measurement environment.

The intent of the present paper is quite different from [1, 11–13], and we show how the plasmon propagation properties of the waves can be extracted from the leakage radiation

using a single defocused objective lens for both excitation and detection. Hohenau *et al* [12] made use of sample defocus by observing that intermediate planes between the BFP and the image plane allowed a gradual transition between spatial localization and observation of the *k*-vector. In the present paper, we show that the arrangement of excitation and detection allows both spatial and spatial frequency information to be obtained at a single defocus plane. This arises from the interference between counter propagating waves as discussed later.

2. Experimental arrangement

Figure 1(a) shows the simplified conceptual diagram of the experimental system and figures 1(b) and (c) show typical distributions in the BFP respectively before and after applying a pupil mask to enhance the contribution from the SPs. Figure 1(d) shows the complete optical system with the SLM conjugate to the BFP of the microscope objective.

The BFP of the microscope objective (Nikon, CFI Apo TIRF 60x H, NA 1.49) was illuminated with a linear polarized beam. Key to our method is to generate counter-propagating waves, in order to achieve this, it is necessary to move the sample closer to the objective as shown in figure 2(a). In order to defocus the excitation beam the simplest thing to do is to move the sample mechanically. In our experiment we used the phase-SLM (Holoeye Pluto, Reflective, 1920 × 1080, 256 Grey Levels) conjugate with the BFP with appropriate phase profile to effectively defocus the sample [8]. Moreover, since the radial position in the BFP corresponds to the angle of incidence of the emitted and detected radiation the SLM also gives us precise control in the range of angles for sample excitation. We use annular excitation as shown in figure 1(c); this covers the range of angles over which the SPs can be excited. This ensures that background light incident far away from the SP excitation angle that would obscure the measurement is blocked. The SLM is not essential in the present setup since mechanical defocus could be combined with a fixed mask to form the amplitude pupil function to control the incident angles on the sample. The method thus lends itself to removal of the relatively expensive SLM, however, it is included here both for convenience and to allow comparison with SLM based systems developed in our laboratory. If mechanical defocus were used, precise knowledge of the defocus position is not required since the results are not sensitive to the exact defocus value.

Under these conditions we may envisage that the SPs are excited on a ring which propagates through the optical axis continuously reradiating into light. The decaying profile is depicted schematically with the dashed red lines of figure 2(a). It is worth pointing out that in positive defocus the SPs are also generated but they propagate away from the optical axis, so they do not interfere.

The reflected distribution at the BFP is projected to the camera (IDS, UI-3240CP-M-GL), so that the total magnification between the sample and the image plane is 400X, this provides a faithful reproduction of the in plane component of the field on the sample and suppresses axial components of the field since these are only present for TM polarization at large angles of propagation.

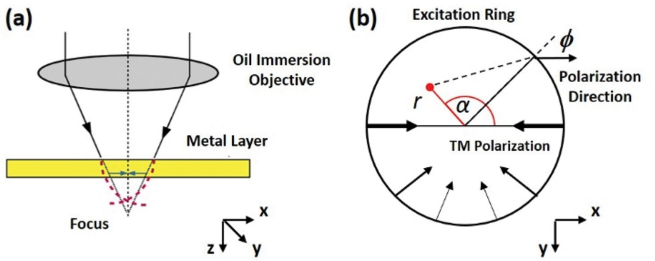

Figure 2. Focusing of surface waves. (a) Schematic diagram showing counter-propagating waves emerging from the points of excitation (side view in plane of TM excitation). The decaying profile is shown (exaggerated) with the dashed red lines. (b) Ring of excitation of SPs on the sample surface arising from defocused objective lens, the parameters φ, α and *r* are used in the analytic calculation of the field (viewed from the top corresponding to the sample surface). It should be noted that the radius of this ring can be predicted with reasonable accuracy from ray theory and increases with defocus.

3. Analytical representation of the field near the optical axis

It may be shown by stationary phase arguments that the defocused beam produces a phase gradient that acts as a unidirectional ring source for excitation of SPs [14] at a radius given by equation (1) provided the distance from focus is more than a few wavelengths. The radius of the ring, *R*, is given by

$$R = \Delta z \, \tan\theta_p \tag{1}$$

where Δz is the sample defocus and θ_p is the angle of excitation and reradiation of the SPs. This radius is the same value as the geometrical optics predictions. We can therefore represent the distribution at the focus as excitation from a ring as shown in figure 2(b).

We now present a simple analytical expression for the field distribution near the focus. We consider the in-plane component of the field which is proportional to the detected leakage radiation in the conjugate image position [12]. The in plane field will clearly have both *x*- and *y*-components that can be separated with the optional polarizer shown in figure 1. If the polarizer is removed as it was for our experiments the intensities of each poarization direction are added. Consider the excitation of inward propagating SPs from a ring as shown in figure 2(b). Since only the TM polarized light excites SPs and the input light is linearly polarized the strength of the SP will vary as $\cos\phi$. The *x*-component of this plasmon field is resolved along *x* to give $\cos^2\phi$. This is indicated by the different strength arrows in figure 2(b). Similarly for the *y*-component we have a weighting of $-\cos\phi\sin\phi = -\frac{1}{2}\sin 2\phi$.

We consider every point on the ring to emit wavelets and recall that the radius of the ring, *R*, is large compared to both the plasmon wavelength λ_p and the radial position, *r*, where we wish to calculate of the field. This assumption amounts to the

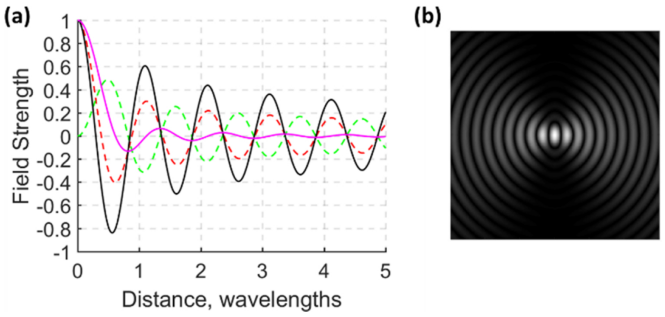

Figure 3. (a) Bessel functions making up the field response of the focusing ring. The red dashed line shows the zero order Bessel function and the green dashed line shows the second order Bessel function. For the x-component these are added to give the magenta solid curve corresponding to TE polarization $\alpha = \pi/2$, which is broadened relative to the zero order Bessel function. subtraction of these curves correspond to TM polarization ($\alpha = 0$), with a narrower distribution and strong oscillations shown by the black solid line. (b) shows the absolute value of the field calculated from equation (3) with the picture width corresponding to ten plasmon wavelengths.

condition that each point on the ring emits a two-dimensional plane wave directed towards the axis. Under these conditions the x-component and y-components of the field, $u_x(r,\alpha)$ and $u_y(r,\alpha)$, may be written as

$$\left.\begin{matrix} u_x(r,\alpha) \\ u_y(r,\alpha) \end{matrix}\right\} = \int_0^{2\pi} \exp[-ikr\cos(\phi-\alpha)] \left\{ \begin{matrix} \cos^2\phi \\ (-\sin\phi\cos\phi) \end{matrix} \right. \mathrm{d}\phi. \tag{2}$$

where $k = \frac{2\pi}{\lambda_p}$. Expanding the cosine squared term and manipulating the integral representations of Bessel functions [15] it may be readily shown that

$$u_x(r,\alpha) = \pi\,[\,J_0(kr) - \cos 2\alpha\, J_2(kr)] \tag{3}$$

where J_0 and J_2 are the zero and second order Bessel functions respectively.

Similarly for the y-component we have

$$u_y(r,\alpha) = \pi \sin 2\alpha J_2(kr)\,. \tag{4}$$

Figure 3(a) shows the Bessel function contributions to equation (3). Figure 3(b) shows the 2D distribution of the absolute value of the field.

It is also informative to consider the asymptotic form of the Bessel functions for large arguments [15], shown below:

$$J_0(kr) \sim \sqrt{\frac{2}{\pi kr}}\cos\left(kr - \frac{\pi}{4}\right),$$
$$J_2(kr) \sim -\sqrt{\frac{2}{\pi kr}}\cos(kr - \pi/4)\,. \tag{5}$$

For the x-component the cosine terms cancel in the vertical and add in the horizontal direction corresponding to TE and TM polarizations respectively. This is shown very clearly in figure 3. Reinforcement of the signal close to the optical axis is associated with cancellation away from the axis and

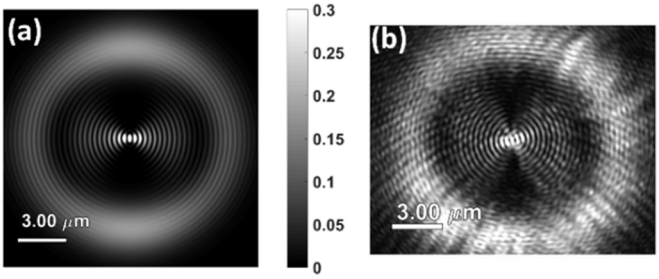

Figure 4. Squared leakage field on the image plane. (a) Simulated and (b) experimental patterns generated at a defocus of −6000 nm for gold with layer thickness of 43 nm and free space wavelength 633 nm (images are saturated at 0.3 of maximum value for better visualization).

vice versa. The TM intensity corresponds to a standing wave with a period of $\lambda_p/2$ away from the center. At the distances used in our experiments the average period is less than 0.5% greater than this value. This factor can be used for correction and, moreover, any relative changes in λ_p are faithfully reproduced. As mentioned earlier a polarizer before the detector can remove the y-component of the field, however, although this is less significant overall than the x-component it does add some intensity signal especially close to the 45° azimuthal positions, so the polarizer was not used in the experiments reported in section 4.

4. Experimental results and numerical simulations

The simulations taken at a defocus of $z = -6000$ nm shown in figure 4, confirm the predictions of the analytic expression close to the focus. They also include the effects of the region where the waves are excited, corresponding to the ring of excitation. There is little signal outside the ring of excitation, which differs from positive defocus where there is little signal close to the optical axis (not shown). The experimental pattern shown in figure 4(b) show similar features.

Based on our analytic formulations and the simulations we can develop a procedure to recover the wavelength of the SPs from the image plane distribution. The signal processing has some parallels with the procedure described in [9], although the physical mechanism for generating the signal is quite different. There are certain conditions we need to fulfil to develop an effective and robust algorithm, with good noise immunity. (i) We wish to use the distribution slightly away from the optical axis where the Gouy phase shift affects the phase distribution. Moreover, we do not use the signal too far from the optical axis where the fringes become weaker. (ii) We should use results over a range of azimuthal angles, even though the strongest signal is directed along the horizontal direction as contributions from other directions greatly enhance the signal to noise ratio, at the end we should obtain a line trace that represents the standing wave pattern of the SPs. (iii) We also need to condition the signal so the slowly varying background is removed and the DC component is zero in order to apply the Hilbert transform. As explained in [9] the Hilbert transform

Table 1. Summary of the experimental results comparing surface profiler, BFP measurement and rapid measurement on the image plane.

	Thickness t (nm)		
Layer	SProf	BFP	Image plane
0	—	—	—
1	7.89	7.846	7.441
2	10.30	10.754	11.344
3	14.21	14.015	13.687

SProf: surface profiler; BFP: back focal plane.

works well for a slowly varying signal with one predominant frequency.

To validate this approach we measured four image plane distributions from 43 nm thick gold samples with different thickness of indium tin oxide (ITO) deposited on the gold. An experimental result corresponding to uncoated gold is shown in figure 4(b), the image shows some irregularity which we attribute to the imperfections in the gold layer, these do not, however, change the underlying frequency of the interference fringes. Similar results were obtained for the coated samples.

We demonstrate the processing of these image distributions with one example and tabulate the results for all the samples in table 1.

Figure 5(a) shows the response from a single horizontal line. There is some saturation of the signal close to the optical axis, but this is not an issue as this data is not used in the final processing. In order to average the signal over a range of azimuthal angles as described in the previous paragraph we rotate the image through a range of angles of typically $-45°$ and $45°$. These projections are added to achieve a plot utilizing signals over a range of propagation directions. In order to perform this operation, it is necessary to have an accurate estimate of the center of the distribution. This can be achieved with a centroiding algorithm. The output from this process is shown in figure 5(b). To remove the DC and slow varying components a wavelet transform is used the output shown in figure 5(c) is filtered by a Morlet wavelet [16]. The filtering does not bias the signal from the four samples since these are well separated from the components we need to remove. We then performed a Hilbert transform on the output of figure 5(c) and extracted the gradient of the phase from the two symmetrical regions shown in the dashed red box of figure 5(d). These regions have good linearity and are far from the optical axis where the Gouy phase shift is apparent. The wavelength of the standing wave pattern is extracted from the phase of the standing wave pattern which will change by 2π for each period. The period of the standing wave pattern is very close to $\lambda_p/2$ the recovered period and can be easily converted to $\lambda_p/2$ by application of equation (2) to determine the precise period at the specific radial position. It is also possible to add the positive and negative output to get a single sided distribution which gives the same results on a uniform sample but not on a spatially varying sample as discussed later.

The same processing was used for the other three image plane distributions obtained with on the coated gold samples

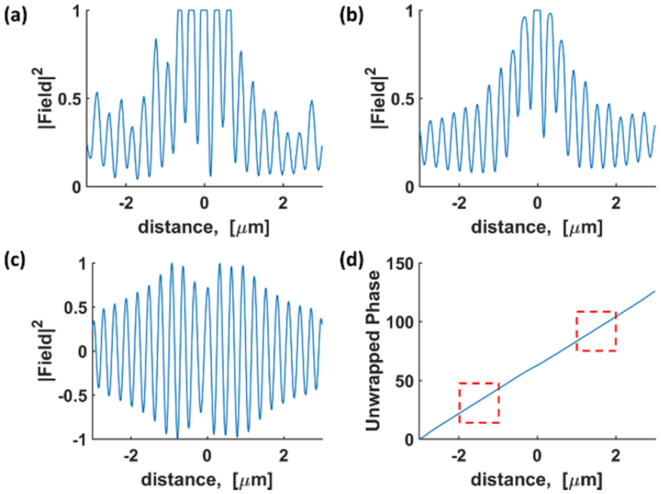

Figure 5. Detailed processing stages. (a) Single line trace on the intensity distribution as a function of distance from the optical axis, (b) the averaged line trace over a range of azimuthal angles (averaging between -45 and $+45°$), (c) filtered line trace by Morlet wavelet and (d) the recovered phase is obtained by taking the phase of the Hilbert transform of the signal in (c) To recover the plasmon k-vector. The red boxes represent the range of defocuses used to extract the surface plasmon k-vector.

with different thickness of layers of ITO. By measuring the k-vector associated with each of the different layered samples the thickness can be recovered once the refractive index of the ITO is inserted. This was achieved using the same process used in [8, 9]; the k-vector of the SP can be calculated from the reflection coefficient for a layered material using the multilayer approach described in [17]. The incident k-vector where the reflected phase is 180° corresponds to the k-vector of the SP. The change in k-vector for different ITO layer thicknesses was calculated using this approach and compared to the measured k-vectors to recover the layer thickness. Table 1 shows a comparison between the recovered thicknesses of the ITO layers using the analysis of the SP wavelength in the image plane compared with measurements obtained by measuring the radial positions of the minimum in the BFP, this corresponds to the sine of the excitation angle from which the k-vector can be obtained using the index of the microscope objective immersion oil [10]. Table 1 also shows the results obtained with a surface profiler scanned from bare gold to the top of the ITO.

5. Discussion of spatial localization and alignment

As mentioned earlier a measure of the surface wave propagation can be obtained directly from the BFP. For a uniform sample as presented in the experimental section both methods give comparable results, as shown in table 1, although location of the dips in the BFP is slightly less precise than measuring the gradient of the phase change. A significant advantage of the image plane approach, presented in this paper, arises when we examine non-uniform samples where image plane analysis

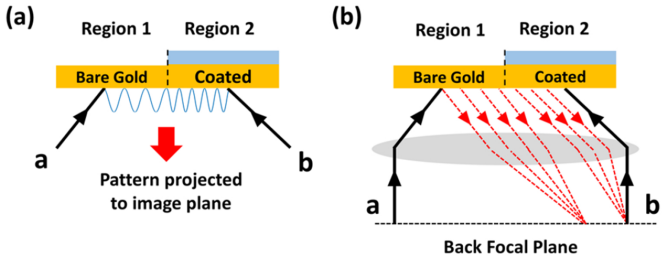

Figure 6. Intuitive explanation of (a) defocused image plane analysis showing that spatial localization occurs within the excitation ring, (b) BFP analysis showing that the measurement is averaged over the excitation region.

is far superior when one wishes to recover the local properties. Indeed, the ability to perform localized measurements on such samples is one of the main motivations for using the microscope objective rather than, say, a prism coupler. A BFP measurement gives spatially averaged measurements, whereas the image plane measurement gives well resolved measurements arising from different parts of the sample. This point may be illustrated with a simple two dimensional picture of the process involved in image and BFP plane measurements respectively. This intuitive picture is then confirmed with rigorous coupled wave analysis (RCWA) which accurately models the measurement process associated with the experimental system. Figure 6(a) represents the situation corresponding to the image plane measurement. Consider illumination where the defocused beam excites SPs on a sample with different SP properties as denoted by the 'bare' and 'coated' gold. The illumination from beams 'a' and 'b' form a standing wave pattern which is projected via leakage radiation to the image plane to form the measurement reported here. The period of the imaged standing wave pattern corresponds to half the wavelength in the observation region. For instance, as the SP excited by beam 'a' crosses from the bare to the coated region its wavelength changes to the value associated with the coated region. The resulting interference pattern is thus localized to the specific position on the sample and the imaging process maps the reradiation from each specific region to the image plane. Now consider figure 6(b) which denotes the situation pertaining to the BFP measurement. The leakage radiation associated with excitation by 'a' will traverse the bare and coated regions and will reradiate at different angles to form a signal at different positions in the BFP, as shown by the dashed red lines. A similar, although not identical situation, arises from the beam associated with excitation by 'b', this is not shown for clarity. It is clear that although reradiation occurs at angles corresponding to the different regions, it is not possible, with an intensity image, to relate the reradiated spot to a specific region on the sample. The BFP measurement forms a weighted average between the bare and coated regions without localization within the illumination area. In most real measurements the difference between the properties of the bare and coated regions is small so the signals overlap.

To confirm these intuitive observations, we performed RCWA [18] simulations on a sample with an 8 μm period binary grating sample consisting of bare gold (4 μm) and coated

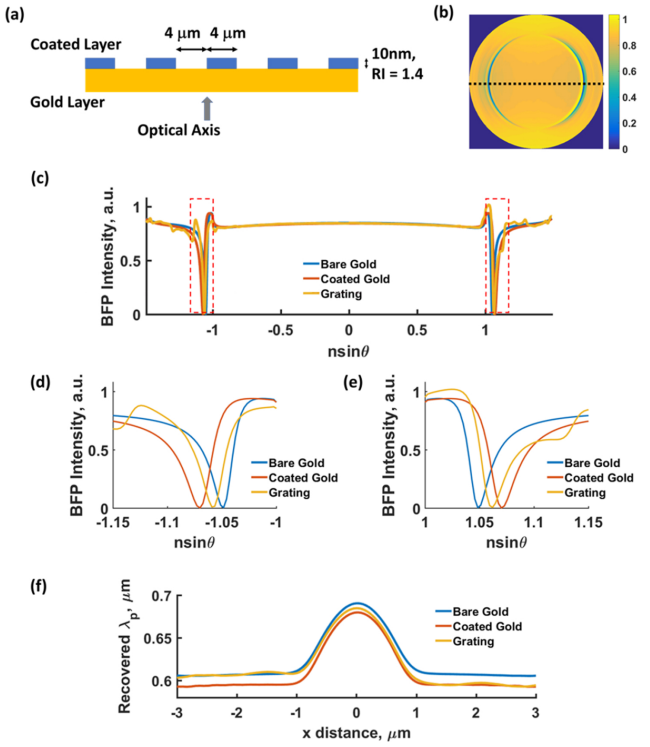

Figure 7. RCWA results with the optical axis at the transition between bare and coated regions, shown schematically in (a). The left and right sides of the incident beam faced bare and coated regions respectively. (b) BFP (intensity). (c) Cross-section of BFP distribution along direction of TM polarization. (d) Expanded profile for left side of BFP and (e) as (d) for right side of BFP. (f) Recovered SP wavelength for image plane analysis.

gold (4 μm) regions, shown schematically in figure 7(a). The coating thickness value used was 10 nm with 1.4 refractive index. The calculation was performed with 51 diffracted orders to achieve convergence. Figure 7(b) shows the BFP response when the optical axis is located at the transition between the bare and coated regions. This means that one side of the image plane distribution involves propagation on the bare region and the other side corresponds to propagation on the coated region. Figure 7(c) shows cross-sections along the TM direction (dashed horizontal line of figure 7(b) of the BFP. Figures 7(d) and (e) show a blown up version of the cross-sections near the SP resonance positions. It can be seen that the dips on the right-and left-hand sides show similar features with a grating response intermediate between the bare and coated regions. The responses on each side are not identical because the beams traverse the bare and coated regions in different orders. Suffice, it to say that these responses make it difficult to localize different areas within the excitation region. On the other hand, figure 7(f) compares the recovered wavelength from the grating sample with uniform layers on the bare and coated regions using the image plane approach reported here. The wavelength was obtained from the calculated phase gradient as a function of position without additional correction. The recovered wavelength from the grating closely follows the bare gold (blue curve) on one side of the grating and on the other side follows the coated curve (yellow). The period of

Table 2. Comparison of SP wavelength λ_p in microns measured on uniform samples and various positions on the grating sample using measurement on the BFP and the image plane.

Sample/Measurement		Recovered λ_p from BFP (μm)	λ_p Contrast from BFP (nm)	Recovered λ_p from ImP (μm)	λ_p Contrast from ImP (nm)
Uniform	Bare	0.6034	12.1	0.6072	12.1
	Coated	0.5913		0.5951	
Grating sample	Bare	0.5982	2.8	0.6085	12.9
	Coated	0.5954		0.5956	

BFP: back focal plane; ImP: image plane

Table 3. Shows the error in film thickness (refractive index 1.5) measurement for 2° tilt along different directions.

β	Error (nm)
0°	+1.57
45°	+1.16
90°	+0.93

the ripples therefore maps the local value of λ_p enabling the spatially varying properties of the SP to be recovered.

Table 2 shows the recovered values of SP wavelengths and more importantly the difference in recovered wavelengths (shown as wavelength contrast) on the coated and uncoated regions. The values were obtained using the annulus between 1 and 2 microns from the optical axis as highlighted in figure 5(d). It can be seen that for the uniform sample both the BFP measurement and image plane measurement give almost the same results. On the grating sample, for the image plane measurements, there is strong contrast between the bare and coated regions, whereas there is little differentiation between the regions with the BFP analysis, showing poor localization as predicted from the intuitive considerations above. In terms of localization, the image plane analysis always outperforms the BFP on heterogeneous samples.

The discussion of localization is, of course, intimately related to resolution. In a typical imaging experiment resolution is largely determined by the ability to separate two distinct points. In a measurement situation the criteria for resolution is more involved since resolution in this case refers to the ability to perform independent measurements on a heterogeneous surface. This corresponds to the ability to perform a measurement in one region without the outcome being disrupted by the value from an adjacent region (we can call this measurement crosstalk) [18]. There is clearly a trade-off between spatial localization and the amount of acceptable crosstalk. It is shown in [18] that the $V(z)$ method gives better resolution compared to direct measurement of the excitation angle in the BFP. In this case crosstalk as high as 20% can be seen for grating periods of 25 μm. For techniques such as $V(z)$ the measurement can be localized to the diameter of the ring of excitation, which in the current experiments was around 12 μm, although it can be smaller with more modest defocus. For the current image plane measurement with the defocused beam the experimental measurements and the RCWA simulations were obtained over a 1 μm patch. While the precise value of localization depends on the acceptable amount of crosstalk and the required signal to noise ratio, it is safe to say that 2 μm resolution with small amounts of crosstalk may be achieved with this method. This validates our assertion that the method can achieve an order of magnitude better SP localization compared to most currently available far field methods. Clearly, further work is required to fully quantify the relative performance of different approaches.

Before concluding this paper it is worth briefly considering the robustness of the measurement to misalignment. We cannot, of course, consider all potential error sources, however, sample tilt or local undulations of the sample are the most significant source of misalignment error. The effects of sample tilt were simulated by considering the change in incident and reflected angles on the sample surface. Table 3 presents the error in film thickness arising from 2° tilt, We consider three tilt directions, β, 0° corresponds to along x-direction (TM polarization), 45° and 90° along the y-direction and tabulate the error in thickness measurement.

As expected tilt along $\beta = 0°$ has a more severe effect than other directions as this directly affects the SP propagation. Our simulations show that the error due to tilt increases quadratically, and since 2° is an extremely large tilt, we may be confident that the system is fairly robust to normal levels of misalignment.

6. Summary and conclusion

We have demonstrated a technique for rapid single shot quantitative measurements of SP wavelength on a local scale by exciting SPs using a defocused microscope objective. Although not discussed here the approach may be readily adapted for the measurement of attenuation. Unlike previous methods the technique does not require change in the defocus position and the full measurement can be obtained with the acquisition of a single image. Moreover, the method lends itself to sensing applications as the whole optical system is separated from the sensing region of the analyte. BFP measurements typically give good measurements of the k-vectors on uniform samples but do not afford good localization. Our discussion shows that the local standing wave pattern allows us to achieve both spatial localization as well as highly precise measurement of the local k-vector on non-uniform samples. The method presented here is thus applicable for precision measurement of local regions of heterogeneous samples in real time. The method shows good resistance to environmental fluctuations compared to interferometric measurements. In addition to the fast measurement capability the optics can be simplified to make a highly compact and inexpensive system.

Funding

This work was supported by the Hong Kong Research Grant Council under research grant PolyU 152478/16E, PolyU 152105/15E and by Hong Kong Polytechnic University under research grant 4-ZZHM and Shenzhen University start up fund.

ORCID iD

Terry W K Chow https://orcid.org/0000-0002-7436-4945

References

[1] Aberra Guebrou S, Laverdant J, Symonds C, Vignoli S and Bellessa J 2012 Spatial coherence properties of surface plasmon investigated by Young's slit experiment *Opt. Lett.* **37** 2139–41
[2] Somekh M G, Liu S G, Velinov T and See C W 2000 Optical $V(z)$ for high resolution 2 pi surface plasmon microscopy *Opt. Lett.* **25** 823–5
[3] Berguiga L, Roland T and Elezgaray J 2011 Amplitude and phase images of cellular structures with a scanning surface plasmon microscope *Opt. Express* **19** 6571–86
[4] Berger C E H, Kooyman R P H and Greve J 1994 Resolution in surface plasmon microscopy *Rev. Sci. Instrum.* **69** 2829–36
[5] Kolmenski A, Kolomenskii A A, Noel J, Peng S and Schuessler H 2009 Propagation length of surface plasmons in a metal film with roughness *Appl. Opt.* **48** 5683–91
[6] Dawson P, Puygranier B A F, Cao W and De Fornel F 1999 The interaction of surface plasmon polaritons with a silver film edge *J. Microsc.* **194** 578–83
[7] Zhang B, Pechprasarn S, Zhang J and Somekh M G 2012 Confocal surface plasmon microscopy with pupil function engineering *Opt. Express* **20** 7388–97
[8] Zhang B, Pechprasarn S and Somekh M G 2013 Quantitative plasmonic measurements using embedded phase stepping confocal interferometry *Opt. Express* **21** 11523–35
[9] Chow T W K, Zhang B and Somekh M G 2018 Hilbert transform-based single-shot plasmon microscopy *Opt. Lett.* **43** 4453–6
[10] Shen M, Learkthanakhachon S, Pechprasarn S, Zhang Y and Somekh M G 2018 Adjustable microscopic measurement of nanogap waveguide and plasmonic structures *Appl. Opt.* **57** 3453–62
[11] Zhu L, Zhang D, Wang R, Wen X, Wang P, Ming H, Badugu R and Lakowicz J R 2017 Out-of-focal plane imaging by leakage radiation microscopy *J. Opt.* **19** 095004
[12] Hohenau A, Krenn J R, Drezet A, Mollet O, Huant S, Genet G, Stein B and Ebbesen T W 2011 Surface plasmon leakage radiation microscopy at the diffraction limit *Opt. Express* **19** 25749–62
[13] Zhang D G, Yuan X C and Bouhelier A 2010 Direct image of surface-plasmon-coupled emission by leakage radiation microscopy *Appl. Opt.* **49** 875–9
[14] Pechprasarn S, Chow T W K and Somekh M G 2018 Application of confocal surface wave microscope to self-calibrated attenuation coefficient measurement by Goos-Hanchen phase shift modulation *Sci. Rep.* **8** 8547
[15] Abramovitz M and Stegun I A 1970 *Handbook of Mathematical Functions* (New York: Dover) ch 9
[16] Büssow M 2007 An algorithm for the continuous Morlet wavelet transform *Mech. Syst. Signal Process.* **21** 2970–9
[17] Azzam R M A and Bashara N M 1977 *Ellipsometry and Polarized Light* (Amsterdam: North-Holland)
[18] Pechprasarn S and Somekh M G 2012 Surface plasmon microscopy: resolution, sensitivity and crosstalk *J. Microsc.* **246** 287–97